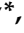




Article

Development of New 14 Cr ODS Steels by Using New Oxides Formers and B as an Inhibitor of the Grain Growth

Alberto Meza ^{1,*}, Eric Macía ¹, Andrea García-Junceda ² , Luis Antonio Díaz ³, Paul Chekhonin ⁴, Eberhard Altstadt ⁴, Marta Serrano ⁵ , María Eugenia Rabanal ¹ and Mónica Campos ¹ 

¹ Department Materials Science and Engineering, IABB, Universidad Carlos III de Madrid (UC3M), Av. de la Universidad 30, 28911 Leganés, Madrid, Spain; eric.macia@uc3m.es (E.M.); mariaeugenia.rabanal@uc3m.es (M.E.R.); monica.campos@uc3m.es (M.C.)

² IMDEA Materials Institute, C/ Eric Kandel 2, 28906 Getafe, Madrid, Spain; andrea.junceda@gmail.com

³ Centro de Investigación en Nanomateriales Y Nanotecnología (CINN-CSIC-UNIOVI-PA), Grupo de Materiales Nanocompuestos y Bioinspirados, Av. de la Vega, 4-6, 33940 El Entrego, Spain; la.diaz@cinn.es

⁴ Helmholtz-Zentrum Dresden-Rossendorf (HZDR), Bautzner Landstraße 400, 01328 Dresden, Germany; p.chekhonin@hzdr.de (P.C.); e.altstadt@hzdr.de (E.A.)

⁵ Materials for Energy Interest Division, CIEMAT, Av. de la Complutense 40, 28040 Madrid, Spain; marta.serrano@ciemat.es

* Correspondence: juanalberto.meza@uc3m.es; Tel.: +34916249482

Received: 4 September 2020; Accepted: 2 October 2020; Published: 8 October 2020

Abstract: In this work, new oxide dispersion strengthened (ODS) ferritic steels have been produced by powder metallurgy using an alternative processing route and characterized afterwards by comparing them with a base ODS steel with Y_2O_3 and Ti additions. Different alloying elements like boron (B), which is known as an inhibitor of grain growth obtained by pinning grain boundaries, and complex oxide compounds (Y-Ti-Zr-O) have been introduced to the 14Cr prealloyed powder by using mechanical alloying (MA) and were further consolidated by spark employing plasma sintering (SPS). Techniques such as x-ray diffraction (XRD), electron backscatter diffraction (EBSD), and transmission electron microscopy (TEM) were used to study the obtained microstructures. Micro-tensile tests and microhardness measurements were carried out at room temperature to analyze the mechanical properties of the differently developed microstructures, which was considered to result in a better strength in the ODS steels containing the complex oxide Y-Ti-Zr-O. In addition, small punch (SP) tests were performed to evaluate the response of the material under high temperatures conditions, under which promising mechanical properties were attained by the materials containing Y-Ti-Zr-O (14Al-X-ODS and 14Al-X-ODS-B) in comparison with the other commercial steel, GETMAT. The differences in mechanical strength can be attributed to the precipitate's density, nature, size, and to the density of dislocations in each ODS steel.

Keywords: ODS steel; mechanical alloying; spark plasma sintering; boron; complex oxides; small punch tests (SP)

1. Introduction

Due to their promising mechanical properties and superior irradiation resistance, over the last decades, oxide dispersion strengthened ferritic steels (ODS FS) have been developed in order to increase the security and thermal efficiency of Generation IV advanced nuclear reactors [1,2]. Their properties are connected to the high precipitates density in the ferritic matrix that not only obstructs the deformation

mechanisms (dislocation movement or grain boundary sliding) but also reduces irradiation effects by being sinks for vacancies and other defects [3–6]. These caused their excellent mechanical behavior under irradiation and high temperatures, leading ODS steels to be suitable for cladding and tubes in the nuclear industry.

The composition in these alloys is a crucial parameter. Every alloying element has a purpose: 14 wt% chromium ensures the ferritic (BCC) nature of the steel and improves its corrosion behavior; Aluminum likewise can enhance corrosion resistance by developing an alumina layer [7] and acts as an oxide former during the consolidation step [8]; Tungsten is an effective element for solid-solution strengthening and promotes high temperature strength [9]; yttrium and titanium are usually included because of their highly reactive nature and their ability to combine with other elements like oxygen to form complex nano-precipitates [10]. A typical composition of ferritic ODS steel is the one used in this research: Fe-14Cr-5Al-3W-0.4Ti-0.25Y₂O₃ [8,11] (wt.%).

However, existing ODS steels need a good balance between their ultimate tensile strength (UTS) and toughness, especially Al containing ODS alloys. Therefore, new strategies must be investigated. Kimura et al. found a small addition (0.6 wt%) of Zr significantly enhanced the creep strength of Al and Ti added ODS steel [7]. Since the ODS steel properties are closely connected to microstructural characteristics, such as the distribution of precipitates and their composition, the method of adding oxide formers to obtain thermally stable nano-oxides is critical. The main preparation route followed in this work is to mechanically alloy (MA) the ferritic steel powder with Y₂O₃ and other oxides formers like Ti. For that reason, this work proposes to synthesize a complex oxide nanopowder by using co-precipitation. This nanopowder would act as a carrier containing all the oxide formers (in this case Y, Ti, and Zr). This method has unparalleled precision to control the precipitate composition compared to traditional MA of pure elements. The new compound is introduced in the milling stage to ensure the formation of an enriched environment regarding these elements. During the subsequent consolidation, nano-oxides form through precipitation [12,13]. Zr is a remarkable addition in this compound, as other authors have reported positive effects such as: refining the oxide particles [14], decreasing the formation of coarse Y-Al-O type oxides, and ensuring there is an elevated dispersion and segregation of the oxides [15,16], thus diminishing grain growth during the consolidation stage [17].

Another goal of the present work is to investigate the influence of boron (B) addition, since B is known to segregate at grain boundaries, inclusions, or precipitates. Boron is a small, reactive element often used to increase the material hardness [18–20] or to improve the creep behavior by inhibiting the coarsening of M₂₃C₆ carbides and stabilizing the carbides fine distributions at grain boundaries [19,21–24]. Another reported feature of B is its ability to activate the sintering process as it promotes the appearance of a liquid phase wetting the surfaces of the powder particles, and thus contributes to an increase in the sintered compact density [25].

Therefore, a significant objective of this work is to develop an alternative processing route with fewer stages, such as posterior heat treatments or thermomechanical treatments, while focusing on strategies that are able to provide an optimum strengthening by using precipitates that limit the formation of coarse Y-Al-O oxides.

The main goal is to study the effect of four different compositions of ODS ferritic steels with different alloying elements additions on the microstructure and, hence, on mechanical behavior, and to compare them with a base material extensively studied previously in the literature [26,27] also processed in this work.

2. Materials and Methods

Four ODS steels were developed following a (powder metallurgy) PM route where powders were mechanically alloyed and further consolidated by spark plasma sintering (SPS) following the compositions listed in Table 1. The initial raw materials were a spherical prealloyed grade Fe-14Cr-5Al-3W (Sandvik Osprey Powder Group, d₅₀ = 30 µm), spherical highly pure Ti powder (GfE mbH, Nuremberg, Germany, d₅₀ = 50 µm), spherical Y₂O₃ powder (TJ Technologies & Materials

Inc., Shanghai, China, $d_{50} = 7 \mu\text{m}$), spherical pure B powder (Good Fellow Cambridge, $d_{50} = 0.9 \mu\text{m}$), and synthesized nanoparticles of a Y-Ti-Zr-O composition.

Table 1. Composition (wt%) of the processed ferritic ODS FS, the Y-Ti-Zr-O compound was synthesized in a lab and its amount was set to maintain an addition of 0.6 wt% Zr.

ODS Steel	Prealloyed				Oxide Formers		Complex Oxide	Other Alloying Elements
	Fe	Cr	Al	W	Y ₂ O ₃	Ti	Y-Ti-Zr-O	B
14Al-Ti-ODS	bal	14	5	3	0.25	0.4	-	-
14Al-Ti-ODS-B	bal	14	5	3	0.25	0.4	-	0.1
14Al-X-ODS	bal	14	5	3	-	-	1.62	-
14Al-X-ODS-B	bal	14	5	3	-	-	1.97	0.1

The synthesis of Y-Ti-Zr-O powders, a compound containing the nano oxides formers responsible for a better precipitation in the ODS steels, was carried out by using co-precipitation involving yttrium nitrate ($\text{Y}(\text{NO}_3)_3 \cdot 6\text{H}_2\text{O}$), titanium isopropoxide ($\text{Ti}(\text{OCH}(\text{CH}_3)_2)_4$) and zirconium n-butoxides ($\text{Zr}(\text{OCH}(\text{CH}_3)_3)_4$) as precursors (all of them were purchased at Sigma Aldrich). Each precursor was mixed by using dissolution individually in different proportions to achieve the desired stoichiometry in 5 ml of isopropanol to avoid unexpected segregations in the next step. After that, the three dissolutions were mixed in an aqueous solution, which was kept at 10 pH through the addition of concentrated NH_4OH at room temperature [28]. The co-precipitation continued for one hour. To remove all the residues produced during the co-precipitation, the resultant precipitated powders were filtered out and washed up several times using distilled water and a mixture of methanol and ethanol in equal proportion (50% in vol.). Subsequently, the powders were dried up in a hot plate and pyrolyzed at 700 °C for one hour in air atmosphere. To crystallize the powders, another heat treatment was performed at 850 °C for 30 min using a heating rate of 10 °C/min in air.

The amount of complex oxide (Y-Ti-Zr-O) was calculated and added to the ODS steels in order to keep the level of Zr at 0.6 wt% equivalent to previous results reported in [29,30].

MA was performed in a horizontal ZOZ Attritor mill Simoloyer CM01 type under a high purity argon atmosphere (99.9995 vol%) after being purged in the vacuum system. Steel balls with a diameter of 5 mm were used, and the balls to powders ratio was 20:1. The rotation speed was set up to be 800 rpm, and the final effective milling time was 40 h for all the compositions. The objective was to involve the same milling energy through the massive collisions, on all 4 ODS FS.

To study the crystallographic parameters of the milled powders, X-ray characterization was carried out in an Xpert Phillips diffractometer (Amsterdam, Netherlands) using $\text{Cu-K}\alpha$ radiation; 2θ -scans were conducted with a step size of 0.02 degree and a step time of 2.4 s. The study of crystallite size and microstrain was performed with the Scherrer Method using Xpert Highscore software (version 2.2.5 Malvern Panalytical, Amsterdam, Netherlands).

A laser particle size analyzer was used (Malvern Mastersizer 2000, Malvern, Worcestershire, UK) to measure the particle size. The powder morphology and microstructures of the alloys were studied by employing scanning electron microscopy (Philips XL-30 and FEI Teneo FEG-SEM, Hillsboro, OR, USA) in combination with TEM (FEI Talos F2000X, Hillsboro, OR, USA) and FEG STEM (FEI Talos F2000X, Hillsboro, OR, USA) for the nano-scale investigations. For TEM examinations, disc-samples of 3 mm in diameter were polished and electropolished at -15°C and 25 V in a solution of 5% perchloric acid in methanol.

A low diffusion sintering technique was selected to consolidate the milled powders while limiting the grain growth in the steels. Samples were sintered by using SPS (FCT System GMBH, HPD25, Frankenblick, Germany). Furthermore, to impede C diffusion from the graphite die, a high-purity (>99.97 wt.%) tungsten foil of 25 μm thickness was used during the sintering process. Subsequently, the milled ODS powders were put in into a 20 mm cylindrical graphite die and heated in vacuum (10^{-2} – 10^{-3} mbar). A sintering temperature of 1100 °C was achieved and maintained for 5 min using a

heating rate of 400 °C/min from room temperature (R.T.), a pressure of 80 MPa was applied in order to obtain samples without pores [29].

The grain microstructure analysis was performed by using different techniques such as SEM (FEI Teneo, Hillsboro, OR, USA) secondary electron (SE FEI Teneo, Hillsboro, OR, USA) imaging and EBSD (Zeiss NVision 40 FEG-SEM equipped with a Bruker EBSD acquisition system, Berlin, Germany). EBSD mappings were done on the transversal section of the consolidated samples by applying a step size between 60 nm and 150 nm. Evaluation was done using an in-house written software; a misorientation threshold of 5 degrees was used for grain determination.

Concerning the study of the nano-sized precipitates, TEM examinations were effectuated using weak beam dark field (WBDF), bright field (BF), STEM, and energy dispersive X-ray spectroscopy (EDX) modes. The precipitates size distributions were determined by measuring the precipitates using the STEM images (3 images per ODS steels) with the image analysis software JMicrovision (version 1.3.3). At least 1000 precipitates were included for each steel specimen.

The mechanical properties were analyzed by measuring Vickers' microhardness (Zwick Roell Microhardness, Indentec Hardness Testing Machines Limited, Southern Avenue, UK), ex-situ micro-tensile tests (Micro Tensile Module, Kammrath and Weiss, Dortmund, Germany) at room temperatures, and small punch tests at both room and high temperatures. For the microhardness measurements, a load of 1.96 N was applied. The $HV_{0.2}$ data corresponds to the average of 20 individual measurements, 10 in the center of the sample and 10 more in the outer part of the considered section. The tensile tests were carried out with miniature T-bone samples, under a strain rate of 2×10^{-3} mm/s, performing 4 tests for every ODS steel. In order to study the fracture mode and ductility, small punch tests with a displacement rate of 0.3 mm/min were performed at room temperature, 300 °C, and 500 °C. For the small punch tests, disc specimens of 3 mm in diameter and with a thickness of 0.250 mm were prepared and finely polished (last step: silica 0.3 µm).

3. Results

3.1. Characterization of Synthesized Complex Oxide

The main objective involving this nano-compound containing the oxide formers (Y, Ti, Zr, O) is to generate environments enriched in these elements once the oxide is decomposed during MA [31].

The crystalline structure of the synthesized Y-Ti-Zr-O nanoparticles was detected by using X-Ray diffraction (Figure 1). In accordance with the published results of Schaedler et al. in [28], a fluorite structure of the powders was identified, together with some minor peaks corresponding to other phases like bixbyte or pyrochlore, which in the end are allotropic phases of fluorite.

Additional examinations of the complex oxide by using TEM and STEM-EDX analysis have been carried out where the exceptionally small (with sizes around 20 nm) flake-shape nanoparticles accumulated as nanoclusters were analyzed morphologically and compositionally (Figure 2).

The EDS analysis conducted using TEM has shown a homogeneous distribution of the four elements over the nano-particles (Figure 3). The composition was determined by using EDS in SEM as $Y_{1.6}Ti_{0.9}Zr_{1.6}O_{7.2}$; this was calculated by taking the average values of each element found in the nano-compound, resulting in this stoichiometry.

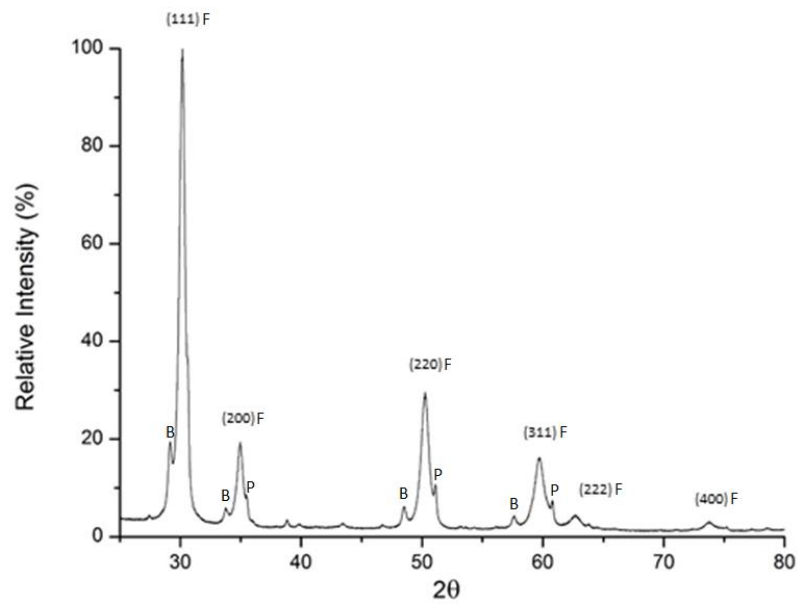


Figure 1. X-ray diffractogram of the synthesized Y-Ti-Zr-O compound after annealing at 850 °C for crystallization.

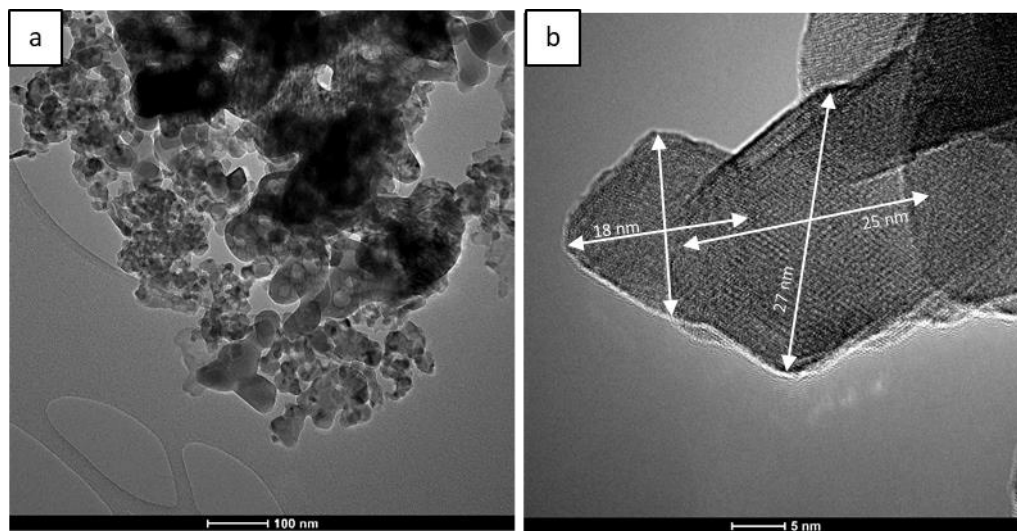


Figure 2. Transmission electron microscopy (TEM) bright field (BF) images of synthesized Y-Ti-Zr-O nanoparticles: (a) agglomeration of Y-Ti-Zr-O particles, (b) detail of the Y-Ti-Zr-O particles.

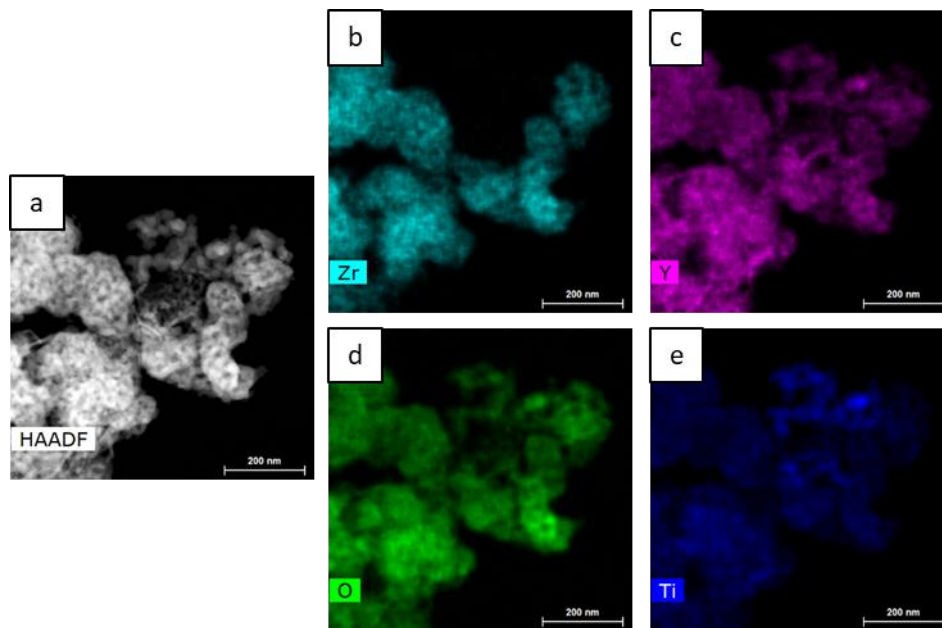


Figure 3. High angle annular dark-field (HAADF) scanning-transmission electron microscopy (STEM) image and corresponding normalized energy dispersive X-ray spectroscopy (EDX) mapping analysis: (a) analyzed area, (b) Zr mapping, (c) Y mapping, (d) O mapping, (e) Ti mapping.

3.2. Characterization of Milled Powders

Powders' morphology and size are shown in Figure 4. After an effective milling time of 40 h for every ODS composition, particles exhibit an irregular morphology, which indicates that a high amount of plastic deformation has been induced in the milled powders during the MA. The particle sizes of the powders are at an adequate range for a proper packing during the SPS consolidation process (see d_{50} in Table 2).

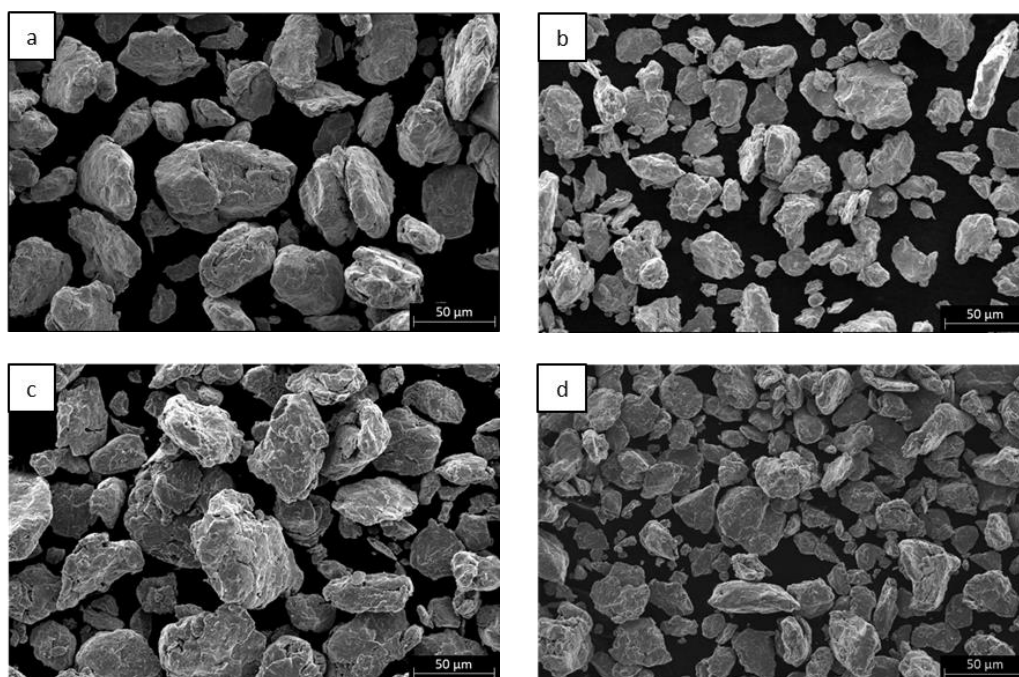


Figure 4. SEM SE images of the milled powders corresponding to the different ODS compositions: (a) 14Al-Ti-ODS, (b) 14Al-Ti-ODS-B, (c) 14Al-X-ODS, (d) 14Al-X-ODS-B.

Table 2. Particle size and crystallographic parameters after using mechanical alloying (MA).

Tag	d ₅₀ (μm)	L (nm)	μ ϵ (%)	Dislocations Density (m ⁻²)	σ_{dis} (MPa)
Preal. powder	30	43.10	0.217	1.07×10^{15}	713
14Al-Ti-ODS	38	11.94	0.769	1.36×10^{16}	2522
14Al-Ti-ODS-B	73	11.99	0.767	1.45×10^{16}	2598
14Al-X-ODS	38	11.60	0.790	1.51×10^{16}	2655
14Al-X-ODS-B	54	11.40	0.808	1.37×10^{16}	2529

d₅₀: Medium value of the particles size, L: crystallite size, μ ϵ : Microstrain level.

It is necessary to characterize the structural features of the milled powder, since they can limit the electrical conductivity and, hence, sinterability by SPS can be compromised [31]. However, if dislocation density remains high after sintering, the contribution to the final hardening can be a positive factor. To calculate the dislocations density (see Equation (1)), the microstrain level and b (Burgers' vector) were considered:

$$\rho_{dis} = 14.4 \frac{\epsilon^2}{b^2}. \quad (1)$$

Compared to base prealloyed powder, the crystalline parameters of the milled powders (Table 2) indicate that the density of dislocations increased and, therefore, the crystalline coherence zone diminished, contributing to a decrease of the crystallite size (L). Furthermore, the plastic deformation and alloying process also increased the lattice distortions due to the addition of Y, Ti, or Zr, and consequently, the microstrain endured by the material increased. Guaranteeing high microstrain values ($\mu\epsilon$) after milling is the key to reducing the later crystallite growth that occurs during the consolidation process. Milling time was selected for the four ODS FS compositions to achieve a similar crystallite size and microstrain level. The strengthening factor and the effects on it caused by dislocation density were also calculated by using Equation (2):

$$\sigma_{dis} = M\alpha_d Gb \sqrt{\rho} \quad (2)$$

where M is the Taylor factor (3.06), G is the shear modulus of iron (85 GPa), b is the burger vector (0.252 nm assumed Fe pure lattice), α is a constant ($1/3$), and ρ is the dislocation density [30–34].

3.3. Microstructural Characterization

3.3.1. EBSD Analysis

Inverse pole figures (IPF) with respect to the surface normal direction of the processed ODS steels are shown in Figure 5. SPS samples attained full densification with no visible porosity, as was also accomplished in other works [30]. Another feature to consider is the inhibition of excessive grain growth in the steels thanks to the low sintering times in SPS consolidation.

The formation of a heterogeneous microstructure has been identified in all four ODS compositions. This happened due to the interaction of several factors that prevented the grain growth during consolidation, such as the high induced microstrain level during the milling step, the effect of oxides nanoclusters as pinning points, or the selected SPS consolidation parameters that limited the diffusion rate [34]. Additionally, the unequal induced plastic deformation and alloying distribution achieved during the MA determined the stored energy and the ability of recrystallization. Thus, grains grew up at different rates generating a bimodal microstructure composed of coarse grain areas (size > 1 μm) surrounding ultrafine grain (UFG) colonies (< 1 μm), as observed in Figure 5.

An important aspect to consider is how the materials with the addition of the complex compound Y-Ti-Zr-O (14Al-X-ODS and 14Al-X-ODS-B) not only exhibit bigger areas of these UFG regions, but also that the mean size of both coarse and ultrafine grains decreased (Table 3). This reveals the effectivity of the oxides when pinning the grain boundaries, thus defining the proper final mechanical

response of the materials [8,29]. The coarse grains appear elongated in all four ODS steels; however, there is no definitive preferred elongation direction. This indicates that the grain growth occurred anisotropically and may have been caused by the applied pressure during the consolidation step. Essentially, this observation suggests that the processing of these steels is inhomogeneous on the μm scale.

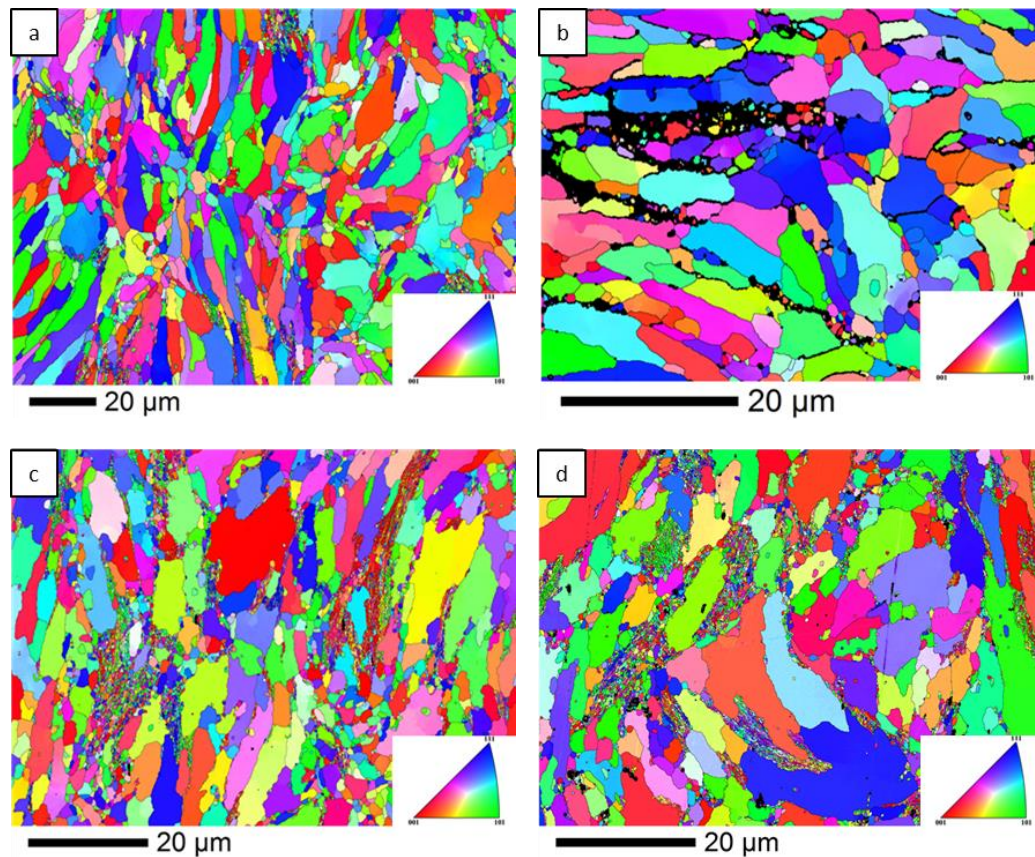


Figure 5. EBSD maps presented as IPFs with respect to the surface normal direction of consolidated ODS steels (be aware of the different magnification) (a) 14Al-Ti-ODS, (b) 14Al-Ti-ODS-B, (c) 14Al-X-ODS, and (d) 14Al-X-ODS-B.

Table 3. Grain distribution for every EBSD map of consolidated ODS steel.

ODS Steel	14Al-Ti-ODS	14Al-Ti-ODS-B	14Al-X-ODS	14Al-X-ODS-B
Mean size of coarse grains ($> 1 \mu\text{m}$)	3.03 μm	2.98 μm	2.48 μm	2.83 μm
Mean size of ultrafine grains ($< 1 \mu\text{m}$)	0.59 μm	0.64 μm	0.26 μm	0.28 μm
% UFG area	5%	13%	13%	16%

Furthermore, the dislocations density of the consolidated materials was calculated (Table 4). It can be observed how the dislocations density decreased after the consolidation of the powders occurred while using SPS. All the materials exhibited values of dislocations and dislocations strengthening in the same order of magnitude.

Table 4. Dislocations density and strengthening based on dislocations of the processed ODS FS.

ODS Composition	Dislocations Density (m^{-2})	Dis (MPa)
14Al-Ti-ODS	3.27×10^{15}	1235
14Al-Ti-ODS-B	2.40×10^{15}	1056
14Al-X-ODS	2.24×10^{15}	1022
14Al-X-ODS-B	2.74×10^{15}	1128

3.3.2. TEM Observations

In order to analyze the nature of the precipitates and their size, TEM examination was carried out in the ODS materials developed, as can be observed in Figure 6. The nano-oxides precipitation took place during the SPS consolidation. TEM images show a proper dispersion of the oxides on the ferritic steel matrix, which granted an additional strengthening due to the dislocations' pinning effect of these precipitates. Several dislocations were also observed inside the grains, which were inherited from the MA processing.

The sizes of the precipitates in all the developed ODS compositions in this work are diverse: the small ones are in the range of 3–10 nm and are located in the interior of the grains. In comparison, the big precipitates exhibit sizes between 60–80 nm and can be found either inside the grains or at the grain boundaries, acting as pinning points (see Figure 6). These last precipitates are, consequently, responsible for preventing excessive grain growth during SPS consolidation. The oxides density was measured and calculated by analyzing the TEM images, which led to obtaining the results shown in Table 5 that are in accordance with those obtained through other investigations [14,29,30]. Additionally, the strengthening coming from the precipitate's dispersion was included in Table 5; this strengthening was calculated using Equation (3):

$$\sigma_{dis} = M\alpha_d Gb \sqrt{N_p D_p} \quad (3)$$

where M is the Taylor factor (3.06), α is a constant ($1/3$), G is the shear modulus of iron (85 GPa), b is the burger vector (0.252 nm assumed Fe pure lattice), N_p is the precipitates density, and D_p is the average precipitate's size [30,34].

By using TEM compositional analysis, the nanoprecipitates were studied. After analyzing the compositional weight percentages in several precipitates, some specific types of precipitates were detected (Table 6). A TEM EDX analysis of the 14Al-X-ODS is shown as an example to describe some characteristics of the ODS compositions containing Y-Ti-Zr-O (Figure 7). As can be observed, Fe and Cr remain stable in the matrix. Another characteristic is the decrease in the quantity of big Ti-W type precipitates in the ODS steels with the addition of the complex compound Y-Ti-Zr-O. Also, Zr tends to react with Ti, forming big precipitates of Ti-Zr. Although other works studied how Zr prevents the formation of Y-Al-O oxides [14], in these steels the presence of the Zr does not completely avoid the formation of the Y-Al-O precipitates; however, it is also remarkable that these precipitates are not as coarse as they otherwise could be (around 80 nm in some cases), thus, the Y-Al-O precipitates exhibit a more refined size with the addition of the complex compound containing Zr. This feature was also observed in previous works conducted by García-Junceda et al. [30].

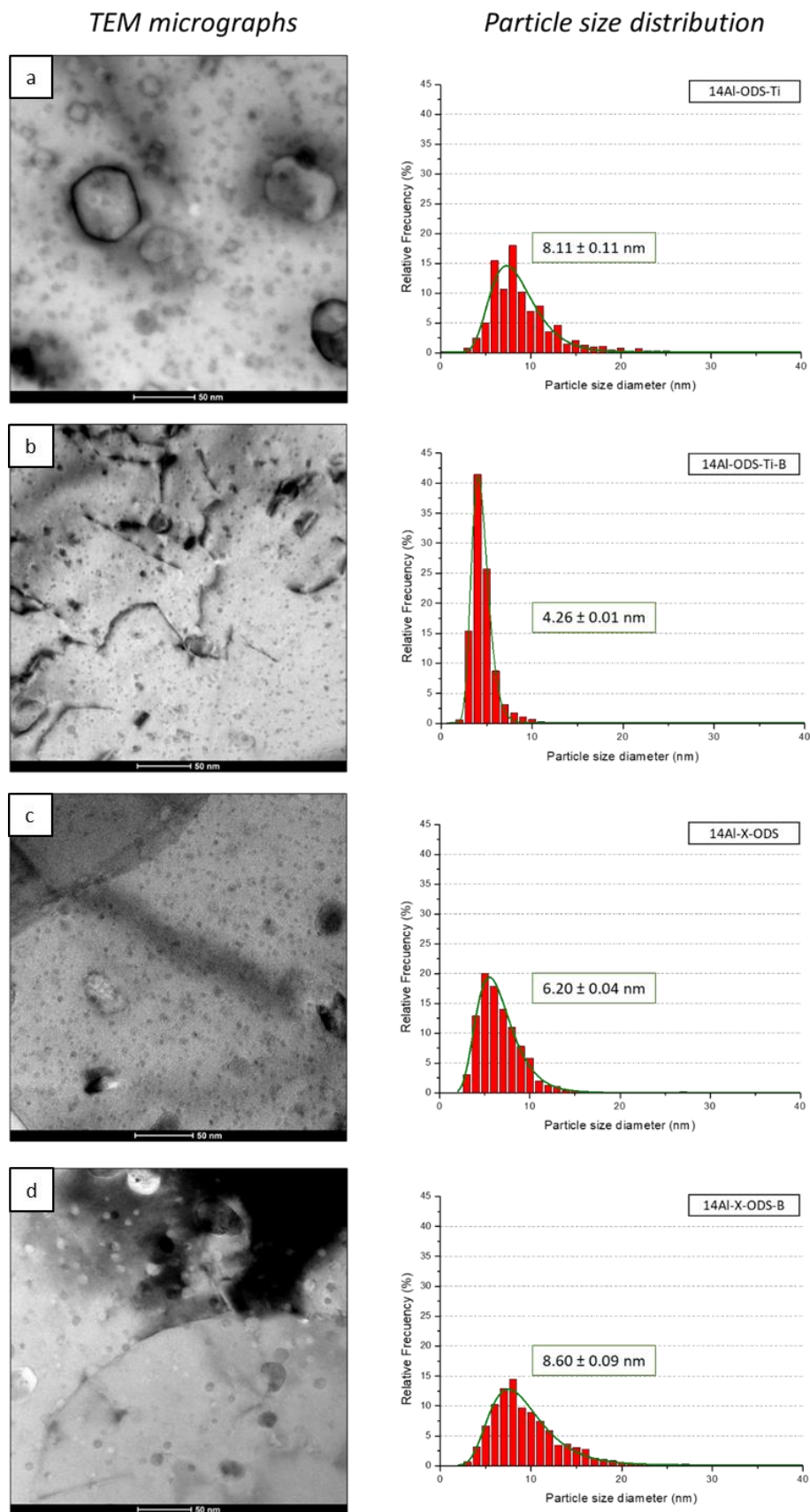


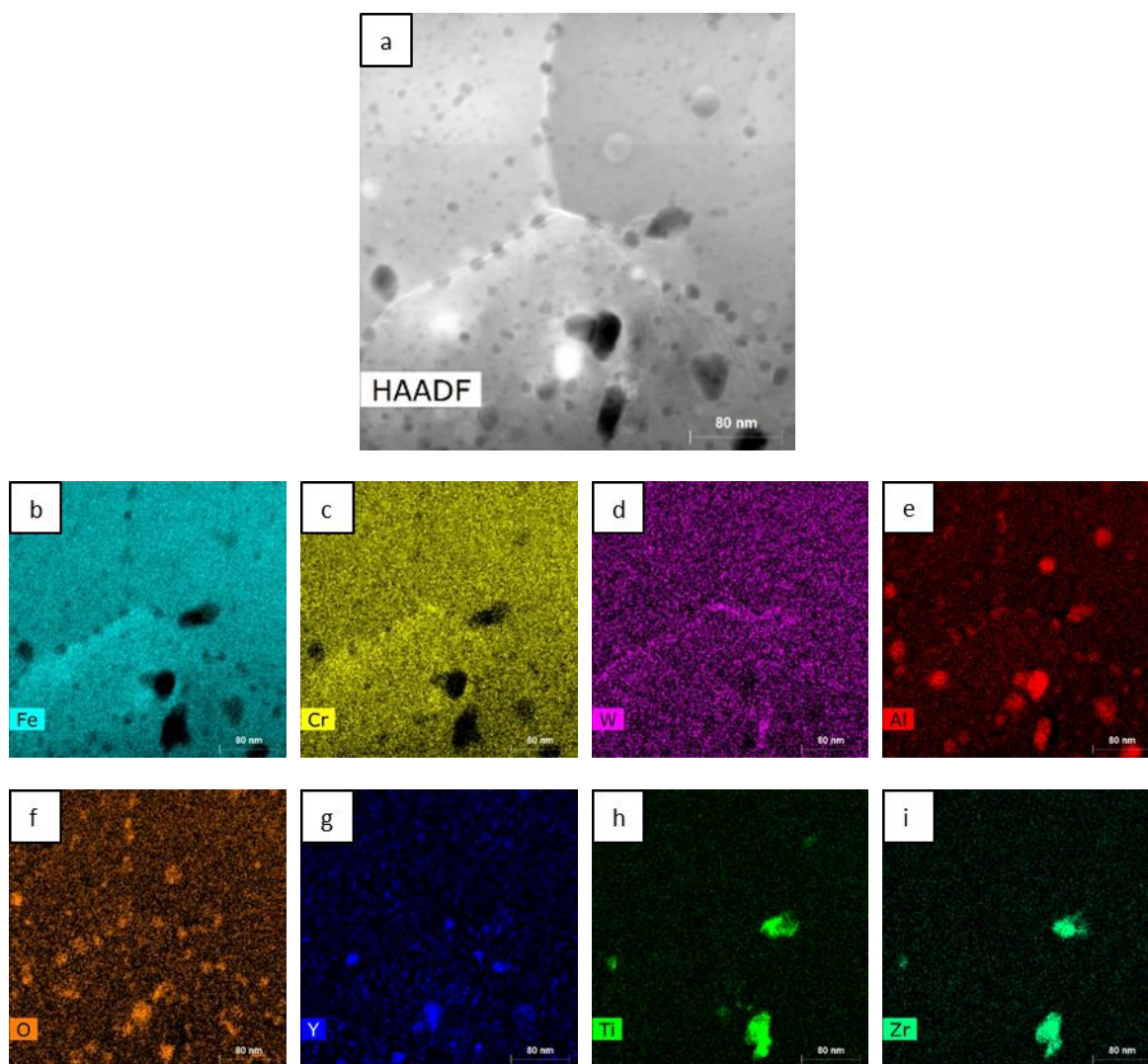
Figure 6. STEM images and precipitates size distributions of the sintered ODS steels: (a) 14Al-Ti-ODS, (b) 14Al-Ti-ODS-B, (c) 14Al-X-ODS, (d) 14Al-X-ODS-B.

Table 5. Precipitates densities for each sintered ODS composition.

ODS Composition	Precipitates Density (Precipitates/m ³)	σ_p (MPa)
14Al-Ti-ODS	2.76×10^{22}	323
14Al-Ti-ODS-B	7.43×10^{22}	384
14Al-X-ODS	4.03×10^{22}	341
14Al-X-ODS-B	1.70×10^{22}	261

Table 6. Detected precipitates in the ODS steels.

ODS Composition	Type of Precipitates				
	Ti-W/Ti-Zr/Ti-Zr-W (60–80 nm)	Y-Al-O (8–20 nm)	Y-Al-Zr-O (6–20 nm)	Y-Al-Ti-Zr-O (6–20 nm)	Y-Zr-O (3–10 nm)
14Al-Ti-ODS	✓	✓	-	-	-
14Al-Ti-ODS-B	✓	✓	-	-	-
14Al-X-ODS	✓	✓	✓	✓	✓
14Al-X-ODS-B	✓	✓	✓	✓	✓

**Figure 7.** EDX Mappings of 14Al-X-ODS: (a) analyzed area, (b) Fe mapping, (c) Cr mapping, (d) W mapping, (e) Al mapping, (f) O mapping, (g) Y mapping, (h) Ti mapping, (i) Zr mapping.

3.4. Mechanical Characterization

In order to test the materials' resistance to plastic deformation, Vickers' microhardness tests were performed for all four ODS compositions (Figure 8). It can be observed how the addition of the Y-Ti-Zr-O significantly reinforced the ODS steels in comparison with the base material (14Al-Ti-ODS), achieving values similar to or even higher than other commercial ODS steels from the literature such as the PM2000 (20 wt% Cr, around 270 HV_{0.2}) or the GETMAT (14 wt% Cr, around 360 HV_{0.2}) [35]. Also, an increase in the microhardness was noticed with the addition of boron to the ODS compositions. Additionally, the low errors obtained in the tests could be associated with the exceptionally good densification of the materials with SPS.

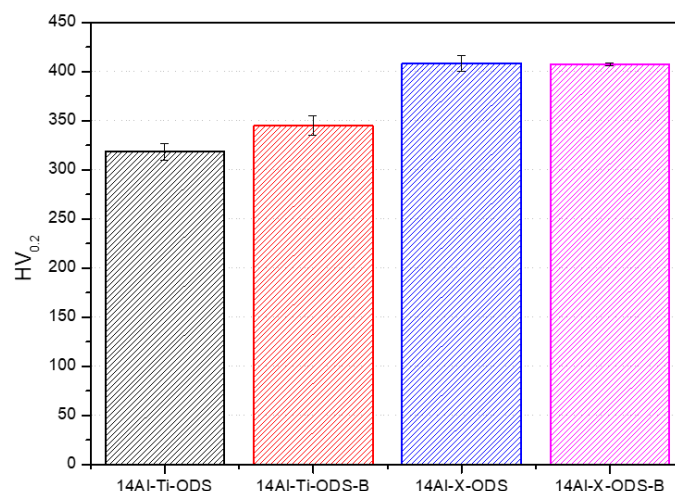


Figure 8. Microhardness results of the developed ODS steels.

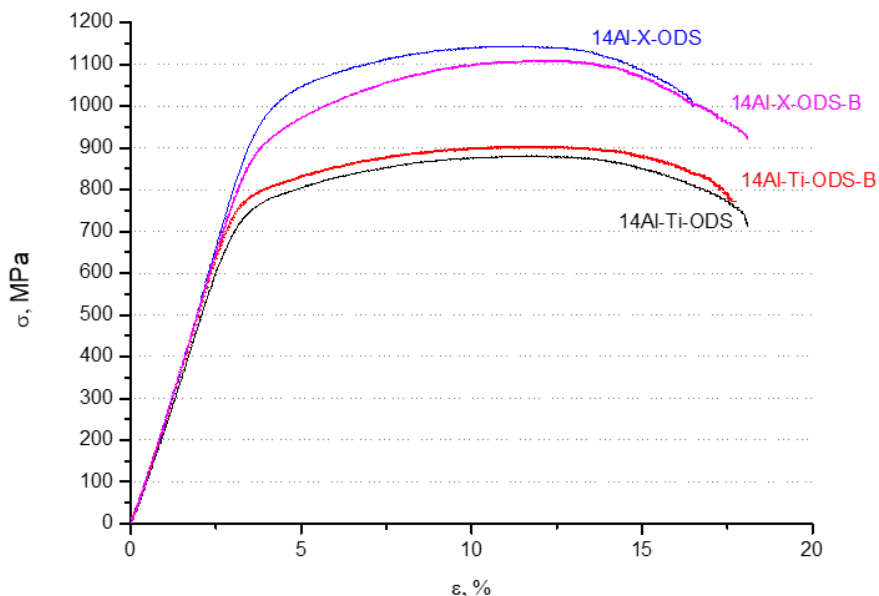
The results of the ex-situ micro-tensile tests are provided in Figure 9. As observed in the tests outcomes, all the materials exhibited superior mechanical properties; specifically, the ODS steels containing the complex compound Y-Ti-Zr-O showed a remarkable increase in their Ultimate tensile Strength (UTS) and their Yield Strength (YS). This could be explained due to the presence of a higher amount of UF grains area, which impedes the movement of dislocations at room temperature. In addition, the total strain endured by the 4 materials resembled their elevated ductility, likewise the toughness (calculated as the area under the tensile stress-strain curve) reached promising values.

An alternative approach is to analyze the influence of composition on mechanical properties under high temperatures by means of SP tests. The SP tests results can be analyzed by using the load-deflection curves shown in Figure 10. Moreover, like in the microhardness measurements, the results were compared to those obtained for GETMAT steel, a widely studied commercial ferritic ODS steel used in similar applications, but with a far more complex processing route involving milling, hot pressing, hot extrusion, and thermal treatments [35]. The GETMAT steel is characterized by the elongated grains product from the extrusion step involved in the manufacturing of these materials, and by the presence of Y-Ti-O precipitates uniformly distributed all over the grains.

The maximum loads withstood by the four ODS compositions can be observed in Figure 11. Although the processed ODS steels underperform in these SP tests at room temperature when compared with the GETMAT, they showed a remarkably improved behavior at high working temperatures (500 °C) by equalizing and in some cases even surpassing the mechanical response of the GETMAT steel. The better response at low temperature of the hot extruded material depends on the fiber texture along the extrusion direction, whereas the SPS steels do not show any texture after the consolidation step. But at higher temperatures, the behavior is linked to other strengthening mechanisms, where precipitates' density, the composition of these precipitates, and their thermal stability all affect the final performance.

In the case of the 14Al-X-ODS and 14Al-X-ODS-B steels, the nature of the precipitated oxides provoked a more effective strengthening than the ODS compositions without Y-Ti-Zr-O, limiting the movement of the dislocations at high temperatures, as seen in the SP results.

Additionally, another feature to take into account is the influence of the grain size (Table 3) in the SP behavior; it can be observed that the ODS compositions with lower grain sizes (both micro and UF grains) exhibited better properties as the test temperature increased.



Tag	UTS/MPa	YS/MPa	Toughness/MPa	Total deformation/%
14Al-Ti-ODS	926 ± 8	757 ± 2	158 ± 26	18 ± 2
14Al-Ti-ODS-B	910 ± 7	790 ± 8	141 ± 38	18 ± 4
14Al-X-ODS	1143 ± 2	884 ± 2	161 ± 23	17 ± 1
14Al-X-ODS-B	1117 ± 8	980 ± 12	166 ± 16	18 ± 1

Figure 9. Comparison of engineering tensile stress-strain curves for the consolidated ODS steels.

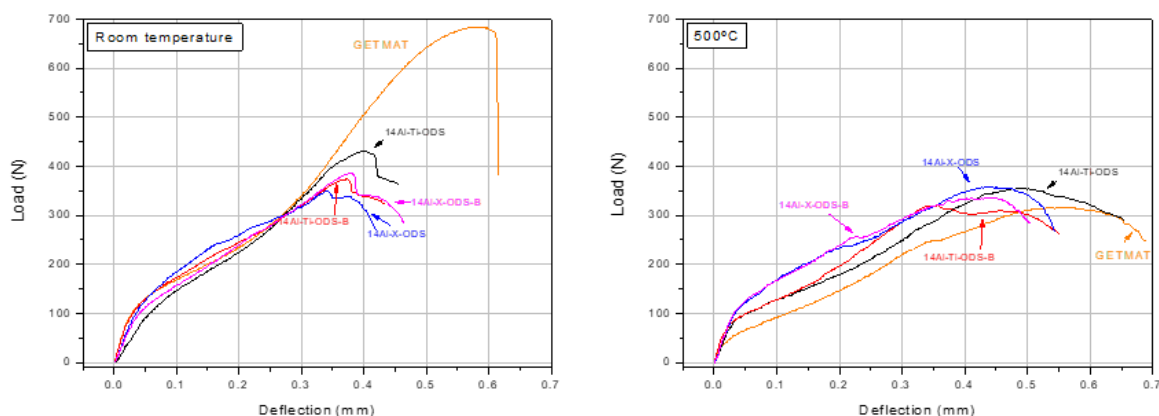


Figure 10. Small Punch tests at room temperature (25 °C) and a high temperature (500 °C).

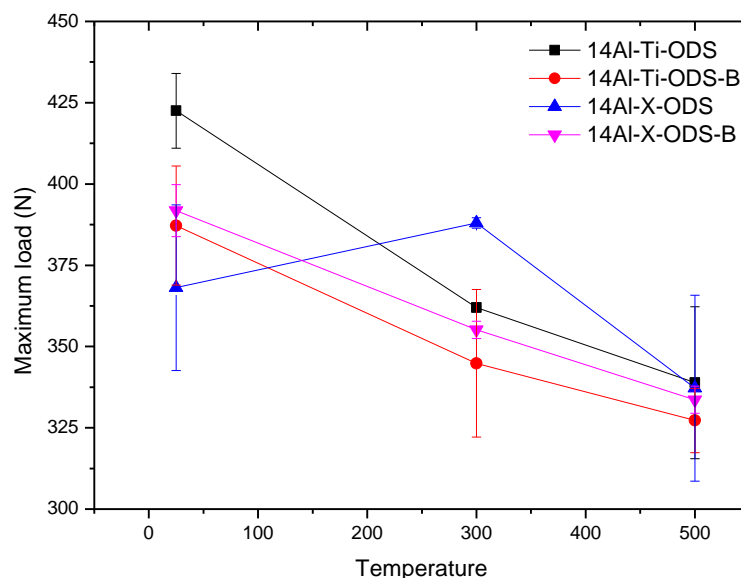


Figure 11. Maximum sustained loads in Small Punch tests performed at room temperature, 300 °C, and 500 °C.

4. Conclusions

In this research, four ODS steels were produced through the addition of a nano complex oxide (Y-Ti-Zr-O) and B. The ODS steels were successfully processed by using MA to mill the powders and by using SPS as a consolidation technique. It is demonstrated that:

- The use of a unique precursor of oxide formers (Y-Ti-Zr-O) resulted in a better control of nano precipitates composition when preparing a F-ODS steel, thereby improving the precipitation of specific oxides containing Zr that led to a strengthened microstructure.
- A good precipitation morphologies (in the order of 10^{22} ox/m³) of the nano oxides was achieved, which may guarantee a fine pinning effect of the oxides over the dislocations and grain boundaries.
- The selected parameters in the SPS technique fully densified the milled powders while avoiding an excessive grain growth during the consolidation stage and maintaining a high density of dislocation. All of this occurred without the necessity of post heat or thermo-mechanical treatments.
- The tailored microstructure affected the final mechanical behavior of the material. The best values of microhardness and UTS were achieved for the 14Al-X-ODS and 14Al-X-ODS-B compositions (with increments of 50 HV_{0.2} and 200 MPa, respectively, in comparison with the reference composition), which were the ones that included the Y-Ti-Zr-O compound in their composition.
- Small punch tests demonstrated the outstanding performance of 14Al-X-ODS and 14Al-X-ODS-B, achieving similar or better results than the GETMAT material when the tests were performed at high temperatures.
- The mechanical behavior of the materials evaluated at room and high temperatures (500 °C) showed very promising and optimum values, comparable to the ones obtained in ODS steels developed with a more complex route.

Author Contributions: Conceptualization, M.E.R., E.M., and M.C.; methodology, A.M., E.M., and M.C.; software, A.M., E.M., M.C., and P.C.; validation, A.M.; formal analysis, A.M., E.M., A.G.-J., P.C., E.A., and M.C.; investigation, A.M., E.M., and M.C.; resources, A.M., A.G.-J., L.A.D., P.C., E.A., and M.S.; data curation, A.M.; writing—original draft preparation, A.M.; writing—review and editing, A.M., E.M., M.E.R., and M.C.; visualization, A.M.; supervision, M.E.R. and M.C.; project administration, M.C.; funding acquisition, M.C. All authors have read and agreed to the published version of the manuscript.

Funding: This research was funded by the Ferro-Ness project and Ferro-Genesys project funded by MINECO under the National I+D+I program MAT2016-80875-C3-3-R and MAT2013-47460-C5-5-P.

Acknowledgments: The authors gratefully acknowledge the help received from Daniel Plaza López during the Small-Punch tests.

Conflicts of Interest: The authors declare no conflict of interest.

References

1. Klueh, R.; Shingledecker, J.; Swindeman, R.; Hoelzer, D.T. Oxide dispersion-strengthened steels: A comparison of some commercial and experimental alloys. *J. Nucl. Mater.* **2005**, *341*, 103–114. [\[CrossRef\]](#)
2. Kimura, A.; Ukai, S.; Fujiwara, M. Oxide Dispersion Strengthening Steels R&D for Advanced Water-Cooling Nuclear Systems. In Proceedings of the ICAPP, Pittsburgh, PA, USA, 13–17 June 2004; ISBN 0-89448-680-2.
3. Lu, C.; Lu, Z.; Xie, R.; Liu, C.; Wang, L. Microstructure of HIPed and SPSed 9Cr-ODS steel and its effect on helium bubble formation. *J. Nucl. Mater.* **2016**, *474*, 65–75. [\[CrossRef\]](#)
4. Kimura, A.; Sugano, R.; Matsushita, Y.; Ukai, S. Thermal Helium Desorption Behavior in Advanced Ferritic Steels. *J. Phys. Chem. Solids* **2005**, *66*, 504–508. [\[CrossRef\]](#)
5. Dou, P.; Kimura, A.; Okuda, T.; Inoue, M.; Ukai, S.; Ohnuki, S.; Fujisawa, T.; Abe, F. Effects of extrusion temperature on the nano-mesoscopic structure and mechanical properties of an Al-alloyed high-Cr ODS ferritic steel. *J. Nucl. Mater.* **2011**, *417*, 166–170. [\[CrossRef\]](#)
6. Zhang, G.; Zhou, Z.; Mo, K.; Miao, Y.; Li, S.; Liu, X.; Wang, M.; Park, J.-S.; Almer, J.; Stubbs, J.F. The comparison of microstructures and mechanical properties between 14Cr-Al and 14Cr-Ti ferritic ODS alloys. *Mater. Des.* **2016**, *98*, 61–67. [\[CrossRef\]](#)
7. Kimura, A.; Kasada, R.; Iwata, N.Y.; Kishimoto, H.; Zhang, C.; Isselin, J.; Dou, P.; Lee, J.; Muthukumar, N.; Okuda, T.; et al. Development of Al added high-Cr ODS steels for fuel cladding of next generation nuclear systems. *J. Nucl. Mater.* **2011**, *417*, 176–179. [\[CrossRef\]](#)
8. García-Rodríguez, N.; Campos, M.; Torralba, J.M.; Berger, M.H.; Bienvenu, Y. Capability of mechanical alloying and SPS technique to develop nanostructured high Cr, Al alloyed ODS steels. *Mater. Sci. Technol.* **2014**, *30*, 1676–1684. [\[CrossRef\]](#)
9. Narita, T.; Ukai, S.; Ohtsuka, S.; Inoue, M. Effect of tungsten addition on microstructure and high temperature strength of 9CrODS ferritic steel. *J. Nucl. Mater.* **2011**, *417*, 158–161. [\[CrossRef\]](#)
10. Boulnat, X.; Perez, M.; Fabrègue, D.; Cazottes, S.; De Carlan, Y. Characterization and modeling of oxides precipitation in ferritic steels during fast non-isothermal consolidation. *Acta Mater.* **2016**, *107*, 390–403. [\[CrossRef\]](#)
11. García-Junceda, A.; Campos, M.; García-Rodríguez, N.; Torralba, J.M. On the Role of Alloy Composition and Sintering Parameters in the Bimodal Grain Size Distribution and Mechanical Properties of ODS Ferritic Steels. *Met. Mater. Trans. A* **2016**, *47*, 5325–5333. [\[CrossRef\]](#)
12. Chen, C.-L.; Richter, A.; Kögler, R.; Talut, G. Dual beam irradiation of nanostructured FeCrAl oxide dispersion strengthened steel. *J. Nucl. Mater.* **2011**, *412*, 350–358. [\[CrossRef\]](#)
13. Rajan, K.; Sarma, V.; Kutty, T.; Murty, B. Hot hardness behaviour of ultrafine grained ferritic oxide dispersion strengthened alloys prepared by mechanical alloying and spark plasma sintering. *Mater. Sci. Eng. A* **2012**, *558*, 492–496. [\[CrossRef\]](#)
14. Dou, P.; Kimura, A.; Kasada, R.; Okuda, T.; Inoue, M.; Ukai, S.; Ohnuki, S.; Fujisawa, T.; Abe, F. TEM and HRTEM study of oxide particles in an Al-alloyed high-Cr oxide dispersion strengthened steel with Zr addition. *J. Nucl. Mater.* **2014**, *444*, 441–453. [\[CrossRef\]](#)
15. Gao, R.; Zhang, T.; Wang, X.; Fang, Q.; Liu, C. Effect of zirconium addition on the microstructure and mechanical properties of ODS ferritic steels containing aluminum. *J. Nucl. Mater.* **2014**, *444*, 462–468. [\[CrossRef\]](#)
16. García-Junceda, A.; García-Rodríguez, N.; Campos, M.; Cartón-Cordero, M.; Torralba, J.M. Effect of Zirconium on the Microstructure and Mechanical Properties of an Al-Alloyed ODS Steel Consolidated by FAHP. *J. Am. Ceram. Soc.* **2015**, *98*, 3582–3587. [\[CrossRef\]](#)
17. Li, W.; Xu, H.; Sha, X.; Meng, J.; Wang, Z. Microstructure and Mechanical Properties of 14Cr-ODS Steels with Zr Addition. *High Temp. Mater. Process.* **2019**, *38*, 404–410. [\[CrossRef\]](#)

18. Moeslang, A.; Klimenkov, M.; Lindau, R.; Materna-Morris, E.; Rolli, R.; Schneider, H.C. Neutron Irradiated Ferritic-Martensitic 9Cr-Steel: Effect of Nanoscaled ODS Particles and Helium Bubbles on Properties. 2016. Available online: https://inis.iaea.org/search/search.aspx?orig_q=RN:47104157 (accessed on 28 February 2018).
19. Abe, F. Effect of Boron on Microstructure and Creep Strength of Advanced Ferritic Power Plant Steels. *Procedia Eng.* **2011**, *10*, 94–99. [\[CrossRef\]](#)
20. Shulga, A.V. A comparative study of the mechanical properties and the behavior of carbon and boron in stainless steel cladding tubes fabricated by PM HIP and traditional technologies. *J. Nucl. Mater.* **2013**, *434*, 133–140. [\[CrossRef\]](#)
21. Abe, F.; Tabuchi, M.; Tsukamoto, S. Mechanisms for boron effect on microstructure and creep strength of ferritic power plant steels. *Energy Mater.* **2009**, *4*, 166–174. [\[CrossRef\]](#)
22. Jayakumar, T.; Mathew, M.D.; Laha, K.; Sandhya, R. Materials development for fast reactor applications. *Nucl. Eng. Des.* **2013**, *265*, 1175–1180. [\[CrossRef\]](#)
23. Abe, F.; Tabuchi, M.; Kondo, M.; Tsukamoto, S. Suppression of Type IV fracture and improvement of creep strength of 9Cr steel welded joints by boron addition. *Int. J. Press. Vessel. Pip.* **2007**, *84*, 44–52. [\[CrossRef\]](#)
24. Abe, F. Progress in Creep-Resistant Steels for High Efficiency Coal-Fired Power Plants. *J. Press. Vessel. Technol.* **2016**, *138*, 040804. [\[CrossRef\]](#)
25. Sulima, I. Role of boron addition on the consolidation and properties of steel composites prepared by SPS. *Bull. Mater. Sci.* **2015**, *38*, 1831–1841. [\[CrossRef\]](#)
26. Torralba, J.M.; Fuentes-Pacheco, L.; García-Rodríguez, N.; Campos, M. Development of high performance powder metallurgy steels by high-energy milling. *Adv. Powder Technol.* **2013**, *24*, 813–817. [\[CrossRef\]](#)
27. Hilger, I.; Boulnat, X.; Hoffmann, J.; Testani, C.; Bergner, F.; De Carlan, Y.; Ferraro, F.; Ulbricht, A. Fabrication and characterization of oxide dispersion strengthened (ODS) 14Cr steels consolidated by means of hot isostatic pressing, hot extrusion and spark plasma sintering. *J. Nucl. Mater.* **2016**, *472*, 206–214. [\[CrossRef\]](#)
28. Schaedler, T.A.; Francillon, W.; Gandhi, A.S.; Grey, C.P.; Sampath, S.; Levi, C.G. Phase evolution in the YO_{1.5}-TiO₂-ZrO₂ system around the pyrochlore region. *Acta Mater.* **2005**, *53*, 2957–2968. [\[CrossRef\]](#)
29. Macía, E.; García-Junceda, A.; Serrano, M.; Hernández-Mayoral, M.; Diaz, L.A.; Campos, M. Effect of the heating rate on the microstructure of a ferritic ODS steel with four oxide formers (Y-Ti-Al-Zr) consolidated by spark plasma sintering (SPS). *J. Nucl. Mater.* **2019**, *518*, 190–201. [\[CrossRef\]](#)
30. García-Junceda, A.; Macía, E.; Garbiec, D.; Serrano, M.; Torralba, J.M.; Campos, M. Effect of Small Variations in Zr Content on the Microstructure and Properties of Ferritic ODS Steels Consolidated by SPS. *Metals* **2020**, *10*, 348. [\[CrossRef\]](#)
31. Hilger, I.; Tegel, M.; Gorley, M.; Grant, P.S.; Weißgärber, T.; Kieback, B. The structural changes of Y₂O₃ in ferritic ODS alloys during milling. *J. Nucl. Mater.* **2014**, *447*, 242–247. [\[CrossRef\]](#)
32. Song, X.; Liu, X.; Zhang, J. Neck Formation and Self-Adjusting Mechanism of Neck Growth of Conducting Powders in Spark Plasma Sintering. *J. Am. Ceram. Soc.* **2006**, *89*, 494–500. [\[CrossRef\]](#)
33. Zhou, X.; Liu, Y.; Yu, L.; Ma, Z.; Guo, Q.; Huang, Y.; Li, H. Microstructure characteristic and mechanical property of transformable 9Cr-ODS steel fabricated by spark plasma sintering. *Mater. Des.* **2017**, *132*, 158–169. [\[CrossRef\]](#)
34. Boulnat, X.; Perez, M.; Fabrègue, D.; Douillard, T.; Mathon, M.-H.; De Carlan, Y. Microstructure Evolution in Nano-reinforced Ferritic Steel Processed By Mechanical Alloying and Spark Plasma Sintering. *Met. Mater. Trans. A* **2013**, *45*, 1485–1497. [\[CrossRef\]](#)
35. García-Junceda, A.; Hernández-Mayoral, M.; Serrano, M. Influence of the microstructure on the tensile and impact properties of a 14Cr ODS steel bar. *Mater. Sci. Eng. A* **2012**, *556*, 696–703. [\[CrossRef\]](#)

